Journal of Materials Chemistry A

Accepted Manuscript

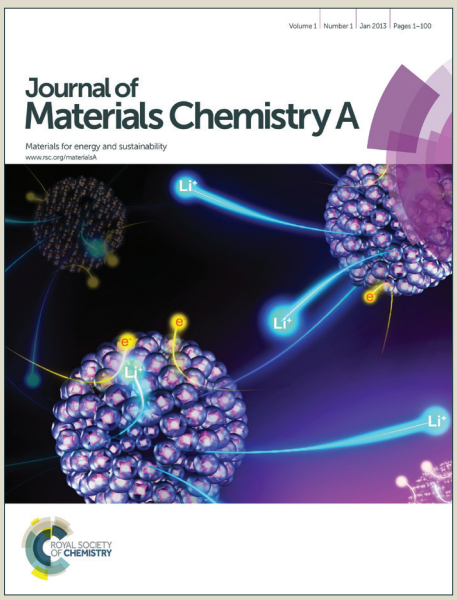

ROYAL SOCIETY OF CHEMISTRY

www.rsc.org/materialsA

Journal Name

RSCPublishing

ARTICLE

In-Situ Synthesis of Mesoporous Single-Grain Layer Anatase TiO_2 Nanosheets without Additives via a Mild and Simple Process for Long-term Li-Ion Battery

Cite this: DOI: 10.1039/x0xx00000x

Received ooth January 2012,
Accepted ooth January 2012

DOI: 10.1039/x0xx00000x

www.rsc.org/

Kunlei Zhu,[a] Xiaoyan Liu,[a] Jiangyong Du,[a] Jianhua Tian,[a] Yun Wang, [b] Shengzhong Liu,[a] and Zhongqiang Shan [a,b*]

There is rare report on mesoporous anatase TiO_2 nanosheets being synthesized without any additives and ex-situ templates at mild conditions. In this paper, mesoporous single-grain layer anatase (MSGLA) TiO_2 nanosheets have been firstly in-situ synthesized without additives in a new methanol-tetrabutyl titanate (TBT) system on a large scale via a simple and easily reproducible method. The formation mechanism of MSGLA TiO_2 nanosheets has been investigated in detail. Our results suggest that MSGLA TiO_2 nanosheets are obtained after a simple thermal treatment for amorphous TiO_2 sheets that are in-situ converted from the precursor $Ti(OC_4H_9)_{4-n}(OCH_3)_n$ ($1 \leq n \leq 4$) (TBM) which is easily gained via transesterification reactions of TBT and anhydrous methanol at room temperature. Moreover, the MSGLA TiO_2 nanosheets are successfully applied as anode materials for Li-ion battery (LIB) and exhibit a discharge capacity of ~ 73 mA h g^{-1} with obvious voltage plateaus over 4000 cycles (a test time of ~ 50 days) at 5 C (1 C=170 mA g^{-1}) and Coulombic efficiency of each cycle approaches 100 %, granting them a promising material for long-term LIB.

1, Introduction

The importance of shaped-controlled synthesis of porous nanostructured materials has cause it to play a role in both the lab as well as in real world applications.[1-3] Mesoporous TiO_2 (with pore diameters of 2- 50 nm) have been extensively investigated owing to their remarkable properties such as tunable pore sizes, high specific surface areas and controllable pore shapes, as well as their fascinating applications including photocatalysis and energy fields.[4-10] Mesoporous TiO_2 are usually synthesized using a soft-templating method[4,8] and hard-templating method[5]. Template-free methods can also fabricate mesoporous TiO_2, but solvothermal treatment and/or additives (i. e. nitric acid) are introduced.[6-10] In all, mesoporous TiO_2 are generally fabricated through solvothermal/ hydrothermal methods under high temperature and high pressure, and/or using templates, organic species and acid as additives, whereas there are few reports of mesoporous TiO_2 being fabricated without any additives and ex-situ template at mild conditions, especially for mesoporous TiO_2 nanosheets.

On the other hand, LIB as a key device for electricity storage has been extensively investigated.[11-13] TiO_2 is a promising anode material for LIB due to its outstanding properties such as environmental benignity, low cost, chemical and structural stability and operation safety. [8,9,14-24] Among numerous forms of titania materials, mesoporous TiO_2 materials have been proved advantageous in Li storage, due to their high porosity and surface area.[20,21] Thus, it is necessary to develop a mild and additive-free method for synthesis of mesoporous TiO_2.

Herein, we originally report a mild, simple and in-situ method for preparation of MSGLA TiO_2 nanosheets on a large scale in methanol without the use of additives (Scheme 1). The formation process of the MSGLA TiO_2 nanosheets has been comprehensively studied. Moreover, the insertion of lithium in the bulk of MSGLA TiO_2 nanosheets has been investigated, indicating them potential anode materials for long-term LIB.

2, Experimental

2.1 Chemicals. Tetrabutyl titanate (TBT, 98%) was bought from Tianjin NO. 1 Chemical Reagent Factory. All alcohols

(chromatographically pure) were purchased from Concord Technology (Tianjin) Co., Ltd. Titanium isopropoxide (TTIP, 98%) and Chloroform-d ($CDCl_3$, 99.8 atom%, with 0.03% (v/v) TMS) was obtained from Beijing InnoChem Science & Technology Co., Ltd. 25 nm anatase TiO_2 particles were purchased from Aladdin (Shanghai) Industrial Inc. The anatase TiO_2 particles were calcined at 500 °C for 2 h before used.

2.2 Preparation of mesoporous anatase TiO_2. Methanol is anhydrous and is confirmed by NMR spectra (Figure S1). In a typical synthesis, 0.5, 1, 2 or 4 ml TBT was immediately added into 18 ml methanol (TBT: methanol molar ratio of ~ 319, ~ 160, ~ 80 and ~ 40) and agitated intensely at room temperature for 24 h to obtain white milky suspension. Dried TiO_2 gel was fabricated after the white suspension was dropped on a Cu or FTO substrate and exposed to air at room temperature for 24 h. Exposure of white milky suspension for 24 h to air aims at two aspects: TBM can sufficiently react with water and the as-prepared product can be dried in air. It is noted that TiO_2 wires and sheets could even be fabricated by the direct addition of water into the white milky suspension. Thus, air humidity is not specially considered here. For comparison, other alcohols (ethanol, n-propanol, isopropanol and n-butanol) replaced methanol while other conditions remained unchanged. Highly crystalline anatase TiO_2 was obtained and any organic components were removed after as-prepared TiO_2 was calcined at 500 °C for 2 h, with a constant heating rate of 2 °C min^{-1}.

2.3 Electrochemical test. The electrochemical tests were performed using 2032 coin cells with lithium as both the counter electrode and the reference electrode. The anode electrode was prepared by mixing the active materials (TiO_2), acetylene black, and binder (PVDF) at a 70:15:15 weight ratio. 1 M LiPF6 dissolved in a 50:50 (v/v) mixture of ethylene carbonate (EC)/diethyl carbonate (DEC) was used as the electrolyte. The slurry of mixture was cast on alumina foil using doctor blade technology, each electrode (14 mm in diameter) containing 1-1.5 mg cm^{-2} of active material. The anode electrode was dried at 120 °C in a vacuum condition (-0.1 MPa) for 12 h, before the cells were assembled in a glove box filled with high-purity argon with concentrations of water and oxygen below 10 ppm. Cyclic voltammetry (1-3 V (vs. Li^+ (1M) /Li), 0.1-2 mV s^{-1}) was carried out using a LK 3 200 electrochemical workstation. The charge-discharge tests were performed using a LAND CT2001A battery test system at different current rates with a voltage window of 1-3 V (vs. Li^+ (1M) /Li). All the electrochemical tests were operated at room temperature.

2.4 Characterization. ^1H NMR spectra were obtained at 25 °C on a VARIAN INOVA 500 MHz spectrometer (USA) using $CDCl_3$ (0.55 ml used in all samples) as solvent. The chemical shift values reported here were calibrated with $CDCl_3$ as a reference. Fourier Transform Infrared (FTIR) spectra were collected on a BIO-RAD 3000 in the range of 4000-400 cm^{-1} using with the KBr pellet technique. Wide-angle X-ray diffraction (XRD) patterns were recorded on a Rigaku D/max 2500 PC diffractometer (Japan) using Cu K radiation at 40 kV and 20 mA. Raman spectra were collected on a DXR Microscope (USA) under a 632.8 nm excitation. The field-emission scanning electron microscopy (FESEM) images and Energy-dispersive X-ray spectroscopic (EDX) analysis were taken with a Hitachi S-4800 microscope (15 KV) equipped with the Thermo Scientific energy-dispersion X-ray fluorescence analyzer. The samples for EDX analysis were directly prepared by dropping the white suspension on a Cu substrate to avoid C element information coming from conductive adhesive which was used for fixing samples. Transmission electron microscopy (TEM) images were captured on a JEOL JEM-2100F microscope (Japan) operated at 200 KV. The samples for TEM measurements were dispersed in ethanol and supported on carbon film coated copper grids. The specific surface area of samples was calculated via the standard multi-points Brunauer-Emmett-Teller (BET) method using a Quantachrome NOVA instrument.

3, Results and discussion

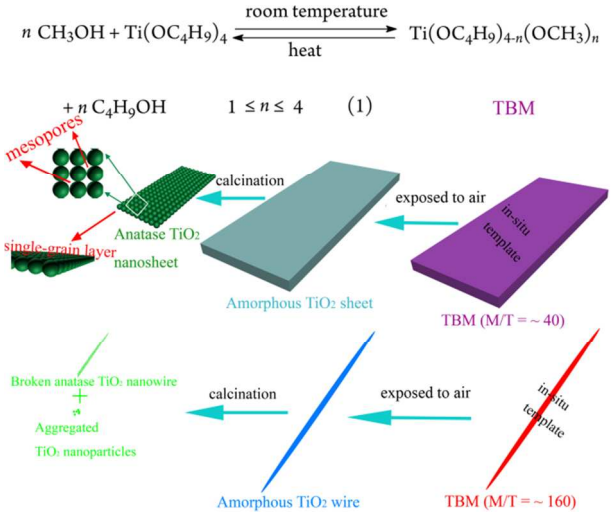

Scheme 1. Synthetic process of mesoporous anatase TiO_2. The illustrations shown in the scheme do not represent the actual sizes of the materials.

The synthetic process of mesoporous anatase TiO_2 is shown in scheme 1. Firstly, the white precipitation precursor TBM can be easily gained by transesterification reactions of TBT and anhydrous methanol (Figure S1) at room temperature. Then, amorphous TiO_2 is in-situ fabricated on a large scale after sufficient hydrolysis of TBM with water in air. Finally, highly crystalline mesoporous anatase TiO_2 composed of nanoparticles can be synthesized after the amorphous TiO_2 samples are calcined at 500 °C for 2 h in air. MSGLA TiO_2 nanosheets are obtained at a low molar ratio of methanol and TBT (M/T), whereas TiO_2 nanowires emerge at a high M/T but some of them are broken.

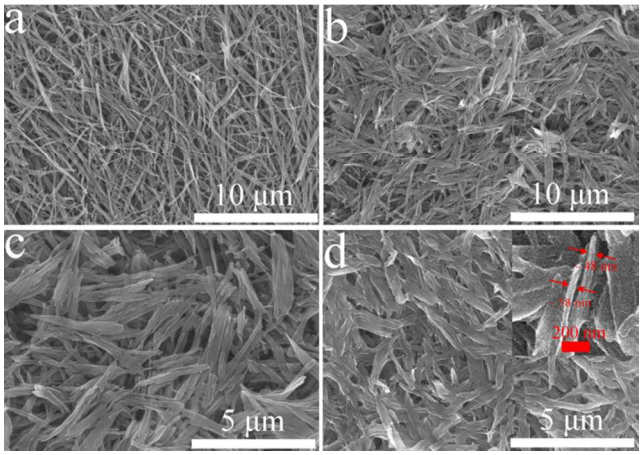

Figure 1. FESEM images of as-prepared TiO_2 wires and sheets with M/T= ~ 319 (a), 160 (b), 80 (c) and 40 (d). Inset: high-magnification FESEM image extracted from Figure 3d. Note: some wires in Fig. 1c are aggregated, but we estimate their size using single wires.

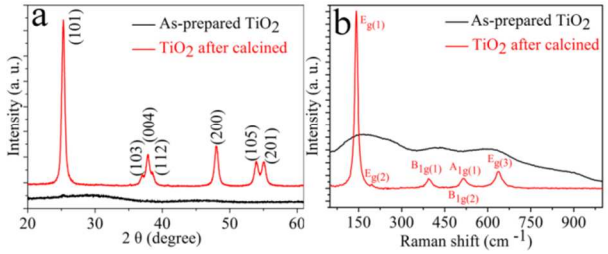

Figure 2. XRD patterns and (d) Raman spectra of as-prepared TiO_2 and calcined TiO_2.

The white TiO_2 xerogel is theoretically produced with 100 % yield on a large scale after hydrolysis of the precursor TBM and drying of the white product at room temperature in air. The field-emission scanning electron microscope (FESEM) images (Figure 1) of the as-prepared TiO_2 xerogel reveal their morphologies varying with M/T. Interestingly, TiO_2 wires appear at a high M/T, whereas TiO_2 sheets emerge at a low M/T. Their sizes are presented in Table S1. Figure 1a and 1b show that the obtained TiO_2 samples are wire-like with a high M/T of ~ 319 and ~ 160. With a decreasing M/T of ~ 80, the length of as-prepared TiO_2 samples reduces, whereas the diameter increases, leading to formation of wider TiO_2 wires (Figure 1c). With M/T decreasing to ~ 40, the as-prepared TiO_2 samples are sheet-like. As shown in Figure 1d, the TiO_2 sheets are predominantly 0.6-3.1 μm in length (~ 1.9 μm on average) and 210-570 nm in diameter (~ 310 nm on average). A careful observation from a high-resolution SEM image (Figure 1d, inset) suggests that the sheets are 40-60 nm in thickness. Thus, it is indicated that the morphology and as-prepared TiO_2 can be easily regulated from wires to sheets by adjusting M/T. The present of Ti and O elements are confirmed by the energy-dispersive X-ray (EDX) spectrum (Figure S2), whereas the as-prepared TiO_2 is amorphous as revealed by the X-ray diffraction (XRD) pattern (Figure 2a, black curve). However, the Raman spectrum (Figure 2b, black curve) displays broad bands at 168, 434, 583 and 902 cm^{-1}. The peak of 168 cm^{-1} resembles the $E_{g(1)}$ and $E_{g(2)}$ (centered around 144 and 197 cm^{-1}) modes of anatase.[26] Being similar with the pattern of anatase, the bands of the sample at 342 and 583 cm^{-1} are assigned to Ti-O stretching mode and the band at 902 cm^{-1} is consistent with the Ti-O stretching mode of Ti nonbonded oxygens.[26] The amorphous TiO_2 is calcined at 500 °C for 2 h in air to obtain highly crystalline anatase TiO_2 and remove any organic components. The crystal phase of calcined TiO_2 is identified using XRD pattern and Raman spectrum. Figure 2a (red curve) shows that all the peaks of the calcined TiO_2 with high crystallinity are indexed to anatase phase (JCPDS card No. 21-1272; space group $I41/amd$; a_o = 0.37852 nm, c_o = 0.95139 nm).[2] The Raman spectrum (Figure 2b, red curve) also indicates that the bands of TiO_2 at 143, 197, 399, 513, 519 (overlapped with the peak of 513 cm^{-1}) and 639 cm^{-1} are designated to six Raman active modes of anatase: $E_{g(1)}$, $Eg_{(2)}$, $B_{1g(1)}$, A_{1g}, $B_{1g(2)}$ and $E_{g(3)}$.[9,27]

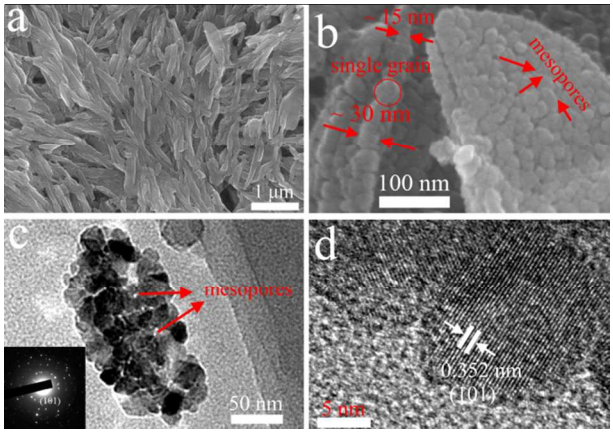

Figure 3. FESEM (a) and high-resolution FESEM (b) images of nanosheets. TEM (c) and high-resolution TEM (d) images of a nanosheet. Inset: SAED of a nanosheet.

After a simple calcination, the amorphous TiO_2 sheets well remain their morphology (Figure 3a) and can crystallize into anatase TiO_2 nanosheets. As shown in Figure 3a, the size of anatase nanosheets is ~ 160 nm average in diameter and ~ 930 nm average in length after calcination, leading to some shrinkage as compared to those of as-prepared TiO_2 (Figure 1d). The high-resolution FESEM image (Figure 3b) suggests that the anatase nanosheets with very rough surfaces consist of 10-30 nm nanoparticles. Moreover, the thickness of anatase nanosheets is 15-30 nm and mesopores with diameter of 6-10 nm are visible among the nanoparticles, indicating the anatase nanosheets are single-grain layer and mesoporous. Transmission electron microscopy (TEM) images (Figure 3c) also clearly present that the anatase TiO_2 nanosheets are composed of 10-30 nm nanoparticles. The nanoparticles connect together, leading to mesopores (5-8 nm) which are randomly distributed among them, as consistent with observation of SEM results. The diffraction rings in the selected area electron diffraction (SAED) pattern (Figure 3c, inset) indicate that the TiO_2 nanosheets are anatase crystalline phase and polycrystalline.[7] Moreover, high-resolution TEM image (Figure 3d) also suggests that the resolution of the lattice fringes of TiO_2 samples are indexed to the (101) facets of anatase TiO_2. In addition, anatase TiO_2 nanowires composed of nanoparticles are obtained after a calcination treatment for amorphous TiO_2 wires, whereas some break into irregular nanoparticles which are serious aggregated (Figure S3). An improved calcination process may be developed to obtain integral nanowires.

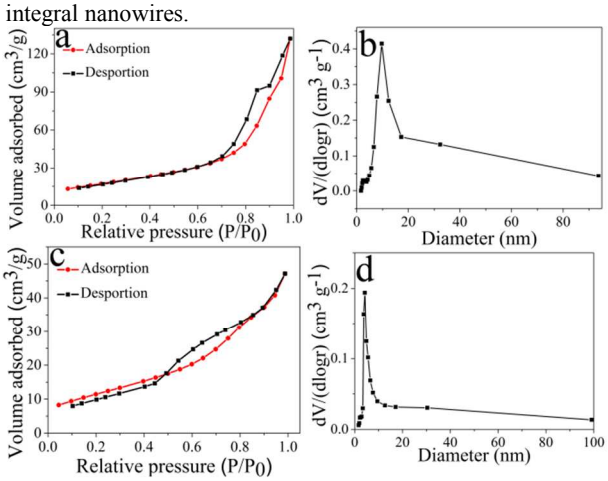

Figure 4. N_2 adsorption-desorption isotherm (a) and the pore size distribution curve (b) calculated by the BJH method of the anatase TiO_2nanosheets. N_2 adsorption-desorption isotherm (c) and the pore size distribution curve (d) calculated by the BJH method of the anatase TiO_2 nanowires.

Figure 4 presents nitrogen adsorption-desorption isotherms and Barrett-Joyner-Halenda (BJH) pore size distribution curves of the anatase TiO_2 nanosheets and nanowires. As shown in Figure 4a, a type Ⅳ isotherm with a type-H3 hysteresis loop at relative pressures of P/P_o= 0.7-1.0 is observed for the MSGLA TiO_2 nanosheets, being representative of mesoporous solids.[2] By the multi-point Brunauer-Emmett-Teller (BET) method, the specific surface area of the nanosheets is obtained to be 62.7 m^2 g^{-1}. The narrow pore size distributions are calculated using Barrett-Joyner-Halenda (BJH) pore size analysis based on nitrogen gas desorption curve. As presented in Figure 3b, the main pore size of the nanosheets is around 9.7 nm, indicating that uniform mesopores exist among the particles of the nanosheets. Thus, SEM observation, TEM analysis and pore size distribution curve all prove that the TiO_2 nanosheets are mesoporous. Moreover, based on SEM and TEM analysis, the TiO_2 nanosheets are composed of relative uniform10-30 nm spherical particles. Thus, the size of basic particles can also be estimated by surface area of the samples. Here, the surface area (S) is correlated with the diameter (d) by the equation: $S = 6/d\rho$, where ρ = 3.89 g/cm^3 is the density of anatase TiO_2. The size of particles of nanosheets is computed to be 24.6 nm, being consistent with analysis of SEM and TEM. Being similar with the nanosheets, the TiO_2 nanowires (including some nanoparticles from ruptured wires during calcination) also display a typical isotherm along two obvious hysteresis hoops at relative pressures of P/P_o=0.5-0.8 and 0.9-1.0 (Figure 4c), suggesting the presence of interparticle, unordered, mesoporosity in the nanowires.[7] The specific surface area of the TiO_2 nanowires is 41.7 m^2 g^{-1} smaller than that of the TiO_2 nanosheets. The pore size distribution curve of TiO_2 nanowires is shown in Figure 4d. The narrow pore size of the TiO_2 nanowires is ~ 6.9 nm less than that of pores (~ 9.7 nm in diameter) in the TiO_2 nanosheets.

In a word, unique mesoporous single-grain layer anatase TiO_2 nanosheets with high crystallinity composed of nanoparticles have been successfully prepared without additive via a simple method.

Surprisingly, only TiO_2 spheres emerge to minimize surface energy[7] if methanol is replaced with ethanol (Figure S4).The special phenomenon appearing in methanol stimulates us to explore the formation mechanism of the MSGLA TiO_2 nanosheets. Firstly, we investigated the component of the white precipitation precursor TBM. When TBT is added into methanol (M/T > 6), the white precipitation TBM could be composite of $Ti(OC_4H_9)_{4-n}(OCH_3)_n$ (n = 1, 2, 3 and 4) produced using methanol as 'precipitant' through multi-step transesterification reactions (reaction 1 in scheme 1) which are reversible when heated. If TBT is replaced with other titanium alkoxides (e.g. titanium isopropoxide), the similar phenomenon emerges. However, no white precipitation, but instead homogeneous solutions are observed, when TBT is added into other monohydric alcohols, such as ethanol, n-propanol, isopropanol and n-butanol. It is suggested that methanol plays a role as 'precipitant' in producing white precipitation $Ti(OCH_3)_4$ via an alcoholysis process [28], whereas other alcohols (e.g. ethanol) are just solvents for TBT. Interestingly, when the reaction solutions are prepared with M/T less than 6, no white precipitation is obtained even after being left to react for more than one year. However, NMR spectrum indicates that some new methyl derivatives,[28] most likely being $Ti(OC_4H_9)_{4-n}(OCH_3)_n$ (n = 1, 2 and 3), are fabricated when the M/T is less than 6. This is discussed in more detail in section 2 of SI.

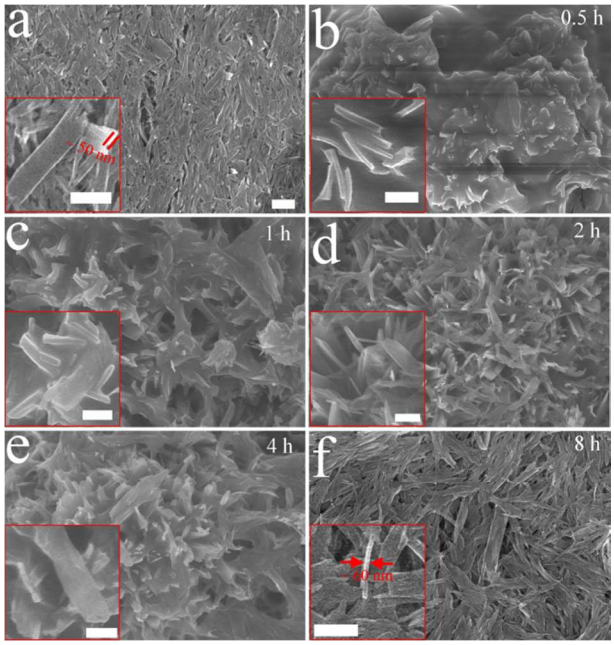

Figure 5. (a) FESEM image of TBM fabricated by reaction solution (M/T = ~ 40) which is stirred for 24 h at room temperature. (b-f) FESEM images of TiO_2 obtained via hydrolysis of TBM fabricated with 0.5-8 h reaction time. The bar is 1 μm. Inset: HR-FESEM images, the bar in inset is 500 nm.

To directly observe morphology of TBM using FESEM, the obtained white precipitation was washed with methanol three times to remove residual TBT and dried in a glove box. The dried TBM was rapidly transferred into the sample chamber of FESEM using a sealed box filled with high-purity argon. Figure 5a suggests that TBM are predominantly sheets ~ 50 nm in thickness, 0.5-2.8 μm in length (~ 1.4 μm on average) and 60-646 nm in diameter (~ 240 nm on average) with a low M/T = ~ 40. The size of TBM is slightly smaller than those of TiO_2 samples (Figure 1d) probably due to methanol washing. Besides, the TBM wires (Figure S5) is similar with the as-prepared TiO_2 wires (Figure 1a), suggesting a probable in-situ conversion from TBM to TiO_2. In order to further explore the roles of methanol and TBM, we investigated morphology of TiO_2 obtained via hydrolysis of TBM precursors which were prepared with different stirring time (M/T= ~ 40). With 0.5 h shorter reaction time, there is small amount of TBM produced and TBT rapidly hydrolyzes with water in air, leading to emergence of TiO_2 bulk (Figure 5b). A careful observation (Figure 5b, inset) indicates that some sheets appear on the surface of TiO_2 bulk. The amount of TiO_2 sheets increases when reaction time is prolonged from 1 h to 4 h (Figure 5c-5e). Furthermore, TiO_2 bulk gradually disappears and sheets tend to grow longer in diameter and length, whereas the thickness of sheets seems to be unchanged. When the reaction time is increased to 8 h, the as-prepared TiO_2 samples are all sheets without bulk seen (Figure 5f). The TiO_2 samples obtained with 8 h have similar morphology with those obtained with 24 h, whereas they have a little smaller size (table S1). Besides, the TiO_2 samples with a high M/T have a similar trend (Figure S6). When the reaction time is 12 h with a high M/T, the transesterification reactions basically finish and sustain a dynamic equilibrium state due to its reversibility. It is suggested that no more TBM is produced, in accordance with our direct observation of white precipitate (Figure S13b). As a result, the TiO_2 maintains an unchanged morphology (Figure S6h and S6i) with reaction time longer than 12 h. It is evident that the TiO_2 bulk/spherical particles are produced from

rapid hydrolysis of TBT when there is little or no amount of TBM within a short reaction time, and the morphology of TiO_2 varies with formation of TBM until the formation of TBM finishes in a dynamic equilibrium state. On the basis of the above analysis, it is concluded that methanol acting as 'precipitant' reacts with TBT to produce TBM which plays a role as an in-situ template for preparation of TiO_2 wires and sheets. In addition, the as-prepared TiO_2 sheets are composed of 3-7 nm grains (Figure S7). During calcination, the grains grow and crystallize into large grains which are basic blocks for the construction of single-grain layer anatase TiO_2 nanosheets, causing pores to form among the grains, ultimately leading to the formation of MSGLA TiO_2 nanosheets.

Altogether, we originally developed a mild, simple, versatile and in-situ method for preparation of mesoporous TiO_2 composed of nanoparticles on a large scale in methanol without any additives (Scheme 1): Firstly, the white precipitation TBM can be easily gained using methanol as 'precipitant' via transesterification reactions of TBT and methanol at room temperature. Then, amorphous TiO_2 is in-situ fabricated on a large scale after sufficient hydrolysis of TBM. The morphology of as-prepared TiO_2 can be easily regulated by varying molar ratio of methanol and TBT (M/T). TiO_2 wires appear at a high M/T, whereas TiO_2 sheets emerge at a low M/T. Finally, highly crystalline MSGLA TiO_2 nanosheets composed of nanoparticles can be synthesized after the amorphous TiO_2 nanosheets are calcined at 500 °C for 2 h in air. In addition, an improved calcination process may be developed to obtain integral TiO_2 nanowires. This synthesis has many advantages: (1) The whole procedure, excluding the calcination treatment is allowed to operate at room temperature in order to remove impurities and get highly crystalline anatase, and no high pressure, ex-situ templates or any organic/corrosive additives are needed, suggesting a real 'green and safe' synthetic process for TiO_2. (2) In this controllable method, the morphology of TiO_2 can be simply changed by varying M/T, indicating a versatile method for 1D and 2D nanostructures. (3) The MSGLA TiO_2 nanosheets are composed of uniform nanoparticles and relatively monodispersed, which facilitates transport of electrons and ions and enables it to suppress some disadvantages for nanoparticles such as uneven pores, poor ionic diffusion and inferior electronic conduction resulting from their serious aggregation.

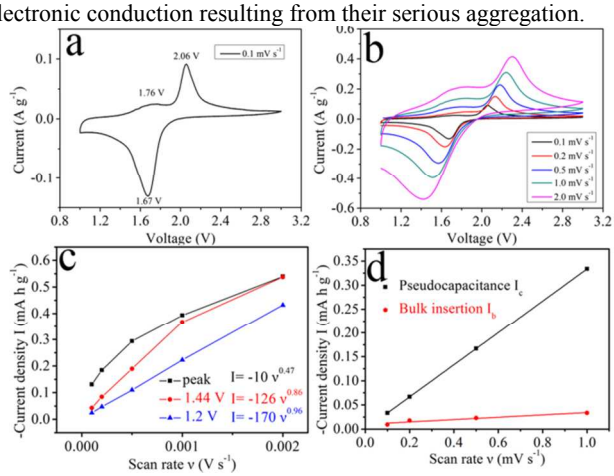

Figure 6. (a) Cyclic voltammetry curve of the MSGLA TiO_2 nanosheets at a sweep rate of 0.1 mV s^{-1}. (b) Cyclic voltammetry curves of the MSGLA TiO_2 nanosheets at different sweep rates. (c) $I=av^b$ curves at cathodic peak, 1.44 and 1.2 V locations for the MSGLA TiO_2 nanosheets. (d) Calculated pseudocapacitive and bulk insertion-related cathodic currents of the MSGLA TiO_2 nanosheets.

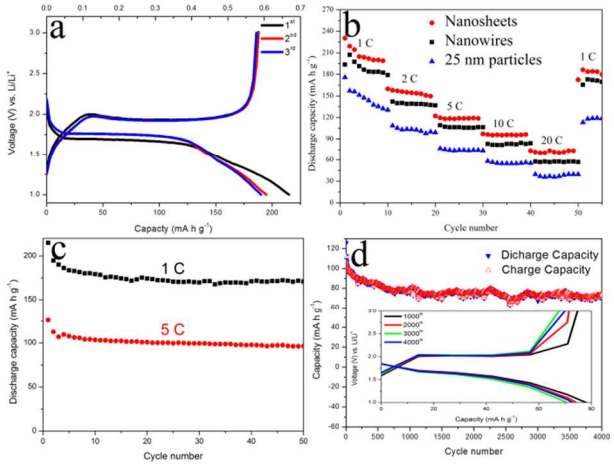

Figure 7. (a) Charge-discharge profiles of TiO_2 nanosheets at 1 C for the first, second and third cycles. (b) Rate capacity curves of TiO_2 nanowires, TiO_2 nanosheets and 25 nm TiO_2 particles. (c) Cycle performance curves of TiO_2 nanosheets at 1 and 5 C. (d) Long-term cycle performance curves of TiO_2 nanosheets at 5 C. Inset: charge-discharge profiles of TiO_2 nanosheets at 5 C for the 1000^{th}, 2000^{th}, 3000^{th} and 4000^{th} cycles.

Although the elongated TiO_2 nanotubular electrode has been prepared with superior cycling capacity over 10,000 cycles,[31] whereas the main capacities are from pseudo-capacitive contribution at high discharge/charge rate.[21,29-31] It is indicated that the reported long-term batteries are actually 'supercapacitors'. Here, we investigated the insertion of lithium into the bulk of MSGLA TiO_2 nanosheets to achieve a long-term Li-ion battery. The anatase TiO_2 generally presents high discharge plateaus at ~ 1.7 V (versus Li^+ (1M) /Li),[22,29] which not only alleviates the formation of solid electrolyte interface layers and avoids electroplating of lithium during charge/discharge process, but also provides constant voltage capacity output. Thus, anatase TiO_2 as a promising choice for Li-ion battery has been widely studied.[8-9,13-25,32-34] Li insertion/extraction into/out anatase can be expressed: $TiO_2 + x\ Li^+ + x\ e^- \leftrightarrow Li_xTiO_2$ with the maximum reversible insertion x= ~ 0.5,[16-17] leading to a capacity of 167.5 mA h g^{-1}.

Figure 6a shows a typical cyclic voltammetry (CV) curve of MSGLA TiO_2 nanosheets at a sweep rate of 0.1 mV s^{-1}. The cathodic and anodic peaks occurring at 1.67 and 2.01V represent the lithium insertion/extraction behavior in the anatase TiO_2, respectively.[22,29] In addition, there is another anodic peak at 1.76 V, whereas its corresponding cathodic peak is not obvious and could be at the range of 1.2-1.67 V probably overlapped by the strong 1.67V anodic peak. The two peaks being likely attributed to surface/interface storage of Li is a pseudocapacitive response as we previously reported.[24] To prove the existence of pseudocapacitive behavior and distinguish the pseudocapacitive contribution to the current response from Li-insertion, we used the reported method of voltammetric sweep rate dependence.[35] The current responses in CV curves (Figure 6b) could be derived from three components: the faradaic contribution from the Li^+ insertion into bulk of TiO_2, the pseudocapacitive contribution involving with storage of Li at TiO_2 surface/interfaces and the non-faradaic contribution from the typical double layer effect. Here, we do not distinguish the double layer capacitance from faradic pseudocapacitance and combine it into pseudocapacitive contributions due to its capacitance value being rather lower than that of faradic pseudocapacitance.[36] These contributions are estimated by investigating the current I obtained from CV curves at various sweep rates v according to[17,35]

$$I=av^b \quad (1)$$

where a and b are adjustable parameters and their value can be determined from the slope of the plot of log v vs log I (Figure S8a-c). There are two well-defined values for b: 0.5 and 1. For b=0.5, the current response in eq 1 is indicative of a faradaic insertion reaction involving a Li diffusion-controlled process. The other defined value, b=1, is representative of a capacitive response. At the cathodic peak of 1.67 V, the b-value is 0.47 (Figure 6c, black curve), indicating that the current is from the Li insertion into the bulk of MSGLA TiO_2 nanosheets process. Ignoring the slight peak shift occurs as a function of sweep rate and we choose two another voltage locations based on CV curve obtained at sweep rate of 0.1 mv s^{-1}. At the location of 1.2 V, the b-value is 0.96 (Figure 6c, red curve), indicating that the current is primarily pseudocapacitive and come from storage of Li at surface/interfaces of MSGLA TiO_2 nanosheets. Interestingly, the b-value is 0.86 (Figure 6c, blue curve) at the location of 1.44 V, suggesting a mixed Li storage process can be expressed at fixed voltage in the following equation:

$$I(V) = k_1v + k_2v^{1/2} \quad (2)$$

where I represents the cathodic current at 1.44 V location, and k_1v and $k_2v^{1/2}$ correspond to the current contributions from the surface pseudocapacitive behavior (I_c) and Li bulk insertion reaction (I_b). We can separate the two contributions by determining k_1 and k_2. For analytical purposes, we rewrite the eq 2 to

$$I(V)/v^{1/2} = k_1v^{1/2} + k_2 \quad (3)$$

The values of k_1 and k_2 can be determined from the slope and the y-axis intercept of the plot of $v^{1/2}$ vs $I(V)/v^{1/2}$ (Figure S8d), respectively. Thus, the I_c and I_b can be can be determined at different sweep rates and used to estimate the relative contribution of surface and bulk storage of Li for the MSGLA TiO_2 nanosheets. As Figure 6d shown, the calculated surface pseudocapacitive currents (I_c) are much larger than Li bulk insertion-related current (I_b) at various sweep rates (0.1-1 mv s^{-1}), indicating that the storage of Li at surfaces/interfaces of MSGLA TiO_2 nanosheets is the predominant contribution at 1.44 V location. However, it is noted that the value of cathodic currents at 1.44 V is much lower than those at cathodic peaks, suggesting Li insertion bulk of MSGLA TiO_2 nanosheets is the principal contribution for the whole storage. Overall, for MSGLA TiO_2 nanosheets, the current comes from bulk insertion process at cathodic voltage peak. The current is pseudocapacitive related to storage of Li on surfaces/interfaces at a lower voltage location (e.g. 1.2V). The current is produced from a mixed process involving contribution of surfaces/interfaces and bulk storage of Li at the middle voltage locations (1.2-1.67 V at the sweep rate of 0.1 mV s^{-1}). For the whole process, Li insertion into the bulk of MSGLA TiO_2 nanosheets is dominating.

Figure 7a presents galvanostatic charge-discharge curves of MSGLA TiO_2 nanosheets electrode for the first few cycles at 1 C (1C= 170 mA g^{-1}) over a voltage range of 1-3 V. Two distinct voltage plateaus at ~ 1.7 V and ~ 1.9 V are characteristic of Li-insertion and Li-extraction, respectively. The first discharge curve of TiO_2 can be divided into three stages. (1) A sharp decrease in voltage from open circuit voltage to ~ 1.7 V. This stage is attributed to formation of solid solution domain of tetragonal anatase ($I4_1/amd$) and Li-poor tetragonal Li$x$$TiO_2$ ($I4_1/amd$) after a small fraction of Li intercalation into the bulk of TiO_2.[19,23] In the MSGLA TiO_2 nanosheets, this corresponds to insertion of 0.048 Li per TiO_2 unit in the tetragonal anatase lattice, leading to formation of Li-poor tetragonal $Li_{0.05}TiO_2$ ($I4_1/amd$). (2) A plateaus zone at ~ 1.7 V is related to two-phase region that Li-rich orthorhombic $Li_{0.5}TiO_2$ (*Imma*) appears and coexists with Li-poor tetragonal Li$x$$TiO_2$ ($I4_1/amd$).[19,22-23,25] In our case, the typical biphase plateau corresponds to Li-rich $Li_{0.4}TiO_2$ coexisting with the Li-poor tetragonal $Li_{0.05}TiO_2$ ($I4_1/amd$). The amount of lithium is ~ 0.35 Li per TiO_2 unit for the MSGLA TiO_2 nanosheets. (3) The last stage is a process of further lithium insertion into bulk and surface/interface of the TiO_2 below 1.7 V. Although more Li (x > 0.5) can be further inserted into the bulk of TiO_2 in this stage, the reaction is known to become sluggish,[13,21] which can be clearly seen from an irreversible capacity of 25.3 mA h g^{-1} in comparison to the first discharge capacity of 214.9 mA h g^{-1} with the subsequent charge capacity of 189.6 mA h g^{-1}.Thus, the irreversible capacity of 25.3 mA h g^{-1} should be related to the further Li insertion into the bulk of MSGLA TiO_2 nanosheets. In addition, there is also reversible Li storage occurring at particles surfaces/interfaces, which is a typical pseudocapacitive behavior.[21-22,24-25] Obviously, the discharge capacity is attributed to both surface/interface and bulk storage of Li, consistent with analysis of CV curves. Nevertheless, the discharge capacities keep a relative constant value of ~ 190 mA h g^{-1} and Coulombic efficiency approaches almost 100% in the second and third cycles due to reversible Li storage at TiO_2 surfaces/interfaces. For the MSGLA TiO_2 nanosheets, there could be ~ 0.076 and ~ 0.165 Li per TiO_2 unit further inserted into bulk and surfaces/interfaces of the electrode materials, respectively. In all, there is ~ 0.641 Li inserted into the MSGLA TiO_2 nanosheets, leading to a discharge capacity of 214.9 mA h g^{-1} for the first cycle. It is noted that the percentage of the amount of lithium in relation with the insertion into the MSGLA TiO_2 nanosheets bulk is ~ 74.3%, indicating the capacity is mainly derived from bulk insertion but not from pseudo-capacitive behavior, agreement with the result from CV analysis. The rate capability curves of TiO_2 samples are presented in Figure 7b. The TiO_2 MSGLA TiO_2 nanosheets show discharge capacities of ~ 200, ~ 160, ~ 120, ~ 100 and ~ 70 mA h g^{-1} at 1, 2, 5, 10 and 20 C, respectively, with a capacity of ~ 180 mA h g^{-1} is still being obtained when the rate is returned to 1 C. It is evident that the capacities of TiO_2 nanosheets are larger than those of TiO_2 nanowires. The reasons are twofold. On one hand, the TiO_2 nanosheets have both a larger specific surface area and pores than those of nanowires (62.7 m^2 g^{-1} *vs* 41.7 m^2 g^{-1} and 9.7 nm *vs* 6.9 nm). The larger specific surface area and mesopores in TiO_2 nanosheets increase the electrode-electrolyte contact area and facilitate electrolyte penetration.[20] On the other hand, some wires crack into seriously aggregated nanoparticles, leading to the formation of uneven pores/voids in the electrodes. Some pores/voids are too small for electrolyte ingress, whereas some pores/voids are too large causing what is believed to be some nanoparticles to peel off from the electrodes during the charge/discharge process.[20] To confirm this hypothesis, ~ 25 nm commercial anatase TiO_2 nanoparticles are introduced after calcined at 500 °C for 2 h. The commercial nanoparticles are serious aggregated (Figure S9), similar to those which are attained from TiO_2 broken wires. As shown in Figure 6b, the discharge capacities of ~ 25 nm TiO_2 nanoparticles are much lower than those of TiO_2 nanosheets and nanowires, probably attributing to serious aggregation of nanoparticles. Figure 7c presents cycle performance of MSGLA TiO_2 anatase TiO_2 nanosheets at 1 C. The discharge capacity keeps a relative constant value of ~ 175 mA h g^{-1} and a Coulombic efficiency of each cycle approaching almost 100 % (Figure S10). A discharge capacity of ~100 mA h g^{-1} is still retained after 50 cycles at 5 C. From the point of view practical applications, a long-term test is a necessary. Therefore, we investigated the insertion of lithium into the bulk of MSGLA TiO_2 nanosheets for a long-term cycle performance test at 5 C. There are two obvious voltage plateaus at ~1.63 V and ~2.02 V during the discharge/charge process (Figure 7d, inset), indicating the capacities mainly originate from lithium insertion/extraction and are not from pseudocapacitance as other electrodes materials.[21,29,37] Figure 7d presents that discharge capacity gradually decreases from ~ 126 mA h g^{-1} to ~78 mA h g^{-1} in the first 1000 cycles, whereas after 1000 cycles, the discharge capacities remain almost unchanged.

After 4000 cycles, a discharge capacity of ~ 73 mA h g^{-1} is still obtained at 5 C and Coulombic efficiency of each cycle approaches almost 100 % (Figure S11), suggesting that anatase TiO_2 is a promising candidate for long-term Li-ion battery. In order to investigate the good cycle performance of the nanosheets, postmortem was conducted after 4000 discharge-charge cycles at 5 C. As displayed in Figure S12, the sheet-like morphology of the TiO_2 nanosheets is generally retained.

The outstanding cycle performance of the MSGLA TiO_2 nanosheets as anode materials for Li-ion battery can be understood from the following reasons: The MSGLA TiO_2 nanosheets composed of basic grains are relatively monodispersed and do not suffer from the aggregation generally existing in nanoparticles. The large specific surface area and mesopores in MSGLA TiO_2 nanosheets shorten diffusion length of electrons and Li ions, providing sufficient space for electrolytes to enter and increase the contact area between electrode and electrolyte; The MSGLA TiO_2 nanosheets with robust frameworks can keep their mesoporous sheet-like structure unchanged during extended Li insertion/extraction process. However, the discharge capacity of the nanosheets is rather poor as compared to other nanomaterials such as ordered mesoporous anatase[20] and anatase nanotubes,[23] probably attributing to their large size in length and diameter which cause a long diffusion distance for Li^+ ions and their disordered porous structure. Although the nanosheets are single-grain layer, the basic grains are 15-30 nm rather larger than those of nanotubes (only 2-3 nm in thickness).[23] However, it should be noted that the downside of nanomaterials-based electrodes is that they exhibit high irreversible capacities especially in the first cycle and are less stable and less densely packed.[13] Besides this, the early study showed an optimum battery performance for $Li_4Ti_5O_{12}$ particles at ~ 20 nm, when at a voltage window of 0.9-2.5 V, with the particles ranging from 1 μm to 9 nm, were used in thin electrode films.[38] It is indicated that the TiO_2 electrode materials may be designed with an optimum particle size in order to obtain high reversible capacities, maintain their stability and obtain high volumetric energy densities. Thus, improved performance would be reached by obtaining integral mesoporous TiO_2 nanowires after an improved calcination process, fabricating mesoporous single-grain layer TiO_2 nanosheets with appropriate sizes via controlling reaction conditions or making ordered pore structure.

4, Conclusions

In summary, we have developed a simple, mild and in-situ method to prepare MSGLA TiO_2 nanosheets without any additives in methanol on a large scale. Our results indicate that the MSGLA TiO_2 nanosheets are able to be obtained by the following steps: Firstly, the TBM precursor can be produced using methanol as 'precipitant' via transesterification reactions and acts as in-situ template for preparation of TiO_2. Then, amorphous TiO_2 sheets are produced at a low M/T after in-situ hydrolysis of TBM. Finally, the amorphous TiO_2 sheets show some shrinkage in sizes and can transform into MSGLA TiO_2 nanosheets after a simple calcination in air. Furthermore, MSGLA TiO_2 nanosheets have been proved to be a promising anode material for long-term battery related to a Li bulk insertion dominating process. However, the anatase TiO_2 materials should be further designed with optimum sizes and high porosity to improve the discharge capacity.

Acknowledgements

This work was financially supported by the National Basic Research Program of China (2015CB251100) and the National High Technology Research and Development Program of China (2013AA050901).

Supporting information for this article is given via a link at the end of the document.

ACKNOWLEDGMENT

We would like to thank professor Chen Ligong and Tian Jun for help with the analysis of ^{1}HMR spectra. We also appreciate the aid of SEM measurement from Jin Fengmin and Wang Huan. We thank Jin Fengmin, Zhu Yingming and Zhang Chen for their generous help with TEM measurement. We are very grateful for English polish from Wayne.

Notes and references

[a] School of Chemical Engineering and Technology, Tianjin University, Weijin Road 92#, Tianjin 300072, P. R. China.
Email: shanzq@tju.edu.cn
[b] National development center of high-technology green materials, Zhongguancun Road 5 #，Beijing 100081, P.R. China.

Electronic Supplementary Information (ESI) available: Pictures, Tables, Reaction equations, ^{1}HMR (500 MHz) spectra, FTIR spectra, EDX spectrum, SEM images, TEM images, SEAD pattern , Coulombic efficiency curves and the exploration of component of TBM are presented. See DOI: 10.1039/b000000x/

1. M. Choi, K. Na, J. Kim, Y. Sakamoto, O. Terasaki and R. Ryoo, *Nature*, 2009, **461**, 246-249.
2. J. S. Chen, Y. L. Tan, C. M. Li, Y. L. Cheah, D. Luan, S. Madhavi, F. Y. C. Boey, L. A. Archer and X. W. Lou, *J. Am. Chem. Soc.*, 2010, **132**, 6124-6130.
3. Y. Deng, J. Wei, Z. Sun and D. Zhao, *Chem. Soc. Rev.*, 2013, **42**, 4054-4070.
4. P. Yang, D. Zhao, D. I. Margolese, B. F. Chmelka and G. D. Stucky, *Nature*, 1998, **396**, 152-155.
5. E. J. Crossland, N. Noel, V. Sivaram, T. Leijtens, J. A. Alexander-Webber and H. J. Snaith, *Nature*, 2013, **495**, 215-219.
6. H. Zhu, X. Gao, Y. Lan, D. Song, Y. Xi and J. Zhao, *J. Am. Chem. Soc.*, 2004, **126**, 8380-8381.
7. D. Chen, L. Cao, F. Huang, P. Imperia, Y.-B. Cheng and R. A. Caruso, *J. Am. Chem. Soc.*, 2010, **132**, 4438-4444.
8. W. Li, Z. Wu, J. Wang, A. A. Elzatahry and D. Zhao, *Chem. Mater.*, 2013, **26**, 287-298.
9. B. Qiu, M. Xing and J. Zhang, *J. Am. Chem. Soc.*, 2014, **136**, 5852-5855.
10. C. Liu, L. Fu and J. Economy, *J. Mater. Chem.*, 2004, **14**, 1187-1189.
11. P. Poizot, S. Laruelle, S. Grugeon, L. Dupont and J. M. Tarascon, *Nature*, 2000, **407**, 496-499.
12. P. G. Bruce, B. Scrosati and J.-M. Tarascon, *Angew. Chem. Int .Ed*, 2008, **47**, 2930-2946.
13. M. Wagemaker and F. M. Mulder, *Accounts. Chem. Res.*, 2012, **46**, 1206-1215.
14. M. Wagemaker, A. Kentgens and F. Mulder, *Nature*, 2002, **418**, 397-399.
15. R. J. Cava, D. W. Murphy, S. Zahurak, A. Santoro and R. S. Roth, *J. Solid State Chem.*, 1984, **53**, 64-75.
16. S. Y. Huang, L. Kavan, I. Exnar and M. Grätzel, *J. Electrochem. Soc.*, 1995, **142**, L142-L144.
17. H. Lindström, S. Södergren, A. Solbrand, H. Rensmo, J. Hjelm, A. Hagfeldt and S.-E. Lindquist, *J. Phys. Chem. B*, 1997, **101**, 7717-7722.
18. A. R. Armstrong, G. Armstrong, J. Canales and P. G. Bruce, *Angew. Chem. Int .Ed*, 2004, **43**, 2286-2288.
19. C. Jiang, M. Wei, Z. Qi, T. Kudo, I. Honma and H. Zhou, *J. Power Sources*, 2007, **166**, 239-243.
20. Y. Ren, L. J. Hardwick and P. G. Bruce, *Angew. Chem.*, 2010, **122**, 2624-2628.

21. J.-Y. Shin, D. Samuelis and J. Maier, *Adv. Funct. Mater.*, 2011, **21**, 3464-3472.
22. J. Liu, J. S. Chen, X. Wei, X. W. Lou and X.-W. Liu, *Adv. Mater.*, 2011, **23**, 998-1002.
23. V. Gentili, S. Brutti, L. J. Hardwick, A. R. Armstrong, S. Panero and P. G. Bruce, *Chem. Mater.*, 2012, **24**, 4468-4476.
24. K. Zhu, J. Tian, Y. Liu, N. Lin, Q. Tang, X. Yu, Y. Zhu and Z. Shan, *RSC Adv.*, 2013, **3**, 13149-13155.
25. W. Li, F. Wang, S. Feng, J. Wang, Z. Sun, B. Li, Y. Li, J. Yang, A. A. Elzatahry and Y. Xia, *J. Am. Chem. Soc.*, 2013, **135**, 18300-18303.
26. P. K. Dutta, P. K. Gallagher and J. Twu, *Chem. Mater.*, 1992, **4**, 847-851.
27. V. Swamy, A. Kuznetsov, L. S. Dubrovinsky, R. A. Caruso, D. G. Shchukin and B. C. Muddle, *Phys. Rev. B*, 2005, **71**, 184302.
28. F. Bischoff and H. Adkins, *J. Am. Chem. Soc.*, 1924, **46**, 256-259.
29. B. Hao, Y. Yan, X. Wang and G. Chen, *Acs Appl. Mater. Interfaces*, 2013, **5**, 6285-6291.
30. H. Liu, Z. Bi, X. G. Sun, R. R. Unocic, M. P. Paranthaman, S. Dai and G. M. Brown, *Adv. Mater.*, 2011, **23**, 3450-3454.
31. Y. Tang, Y. Zhang, J. Deng, J. Wei, H. L. Tam, B. K. Chandran, Z. Dong, Z. Chen and X. Chen, *Adv. Mater.*, 2014, **26**, 6046-6046.
32. Y. Liu, T. Lan, W. Zhang, X. Ding and M. Wei, *J. Mater. Chem. A*, 2014, **2**, 20133-20138.
33. P. Roy and S. K. Srivastava, *J. Mater. Chem. A*, 2015, DOI: 10.1039/c4ta04980b.
34. X.-L. Cheng, M. Hu, R. Huang and J.-S. Jiang, *Acs Appl. Mater. Interfaces*, 2014, 6, 19176-19183.
35. J. Wang, J. Polleux, J. Lim and B. Dunn, *J. Phys. Chem. C*, 2007, 111, 14925-14931.
36. B. Conway, V. Birss and J. Wojtowicz, *J. Power Sources*, 1997, 66, 1-14.
37. V. Augustyn, J. Come, M. A. Lowe, J. W. Kim, P.-L. Taberna, S. H. Tolbert, H. D. Abruña, P. Simon and B. Dunn, *Nature Mater.*, 2013, **12**, 518-522.
38. L. Kavan, J. Procházka, T. M. Spitler, M. Kalbáč, M. Zukalová, T. Drezen and M. Grätzel, *J. Electrochem. Soc.*, 2003, **150**, A1000-A1007.

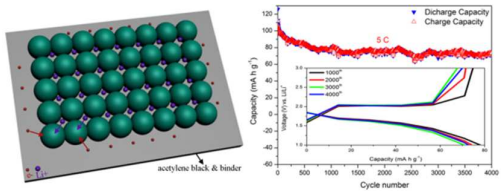

Mesoporous single-grain layer anatase TiO_2 nanosheets have been firstly in-situ synthesized without additives in a new methanol-tetrabutyl titanate system on a large scale via a simple and easily reproducible method and are successfully applied as anode materials for long-term Li-ion battery.